

Laboratory experiments on counter-propagating collisions of solitary waves.

Part 2. Flow field

Yongshuai Chen^{1,2}, Eugene Zhang³ and Harry Yeh^{1,†}

¹School of Civil & Construction Engineering, Oregon State University, Corvallis, OR 97331, USA

²Beijing Aeronautical Science & Technology Research Institute, Beijing, 100083, China

³School of Electrical Engineering & Computer Science, Oregon State University, Corvallis, OR 97331, USA

(Received 16 November 2013; revised 30 June 2014; accepted 21 July 2014;
first published online 19 August 2014)

In the companion paper (Chen & Yeh, *J. Fluid Mech.*, vol. 749, 2014, pp. 577–596), collisions of counter-propagating solitary waves were studied experimentally by analysing the measured water-surface variations. Here we study the flow fields associated with the collisions. With the resolved velocity data obtained in the laboratory, the flow fields are analysed in terms of acceleration, vorticity, and velocity-gradient tensors in addition to the velocity field. The data show that flow acceleration becomes maximum slightly before and after the collision peak, not in accord with the linear theory which predicts the maximum acceleration at the collision peak. Visualized velocity-gradient-tensor fields show that fluid parcels are stretched vertically prior to reaching the state of maximum wave amplitude. After the collision peak, fluid parcels are stretched in the horizontal direction. The boundary-layer evolution based on the vorticity generation and diffusion processes are discussed. It is shown that flow separation occurs at the bed during the collision. The collision creates small dispersive trailing waves. The formation of the trailing waves is captured by observing the transition behaviour of the velocity-gradient-tensor field: the direction of stretching of fluid parcels alternates during the generation of the trailing waves.

Key words: boundary layer separation, solitary waves, surface gravity waves

1. Introduction

A solitary wave that propagates in the x direction can be expressed in terms of the water-surface displacement η as

$$\eta = a \operatorname{sech}^2 \left\{ \sqrt{\frac{3a}{4h_0^3}} \left(x - c_0 \left(1 + \frac{a}{2h_0} \right) t \right) \right\}, \quad (1.1)$$

where a is the wave amplitude, h_0 is the quiescent water depth, c_0 is the wave celerity of ‘linear’ long waves $c_0 = \sqrt{gh_0}$ in which g is the gravitational acceleration, and t is

† Email address for correspondence: harry@engr.orst.edu

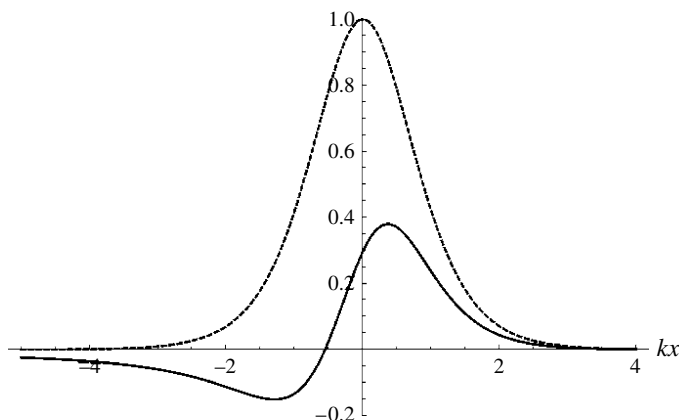


FIGURE 1. Keulegan's (1948) boundary-layer solution $\partial u/\partial z$ at $z=0$, shown by the solid line. The magnitude of $\partial u/\partial z$ is normalized by $\sqrt{\pi\nu/kc_0}/4u_0$ where ν is the kinematic viscosity, k is the wavenumber, and $c_0 = \sqrt{gh_0}$. Dashed line: water-particle velocity profile of the solitary wave $u = u_0 \operatorname{sech}^2 kx$ where we take $u_0 = 1.0$.

time. The solitary wave (1.1) is an exact solution to the Korteweg–de Vries equation, with the assumptions of irrotational flow of inviscid fluid and the wavelength being long in comparison to the water depth.

Unlike the theoretical solitary wave, waves in laboratory experiments are always affected by fluid viscosity. Viscous effects are however confined to near the bottom boundary. Keulegan (1948) presented a theoretical prediction of viscous damping on solitary waves. His solution for the bottom shear stress (or the velocity gradient at the bed) is depicted in figure 1. The solution shows that the bottom shear stress reaches its maximum slightly ahead of the wave crest, and the stress changes its direction in the lee side of the wave. This reversal of the stress remains, even after the passage of the solitary wave, when the water-surface elevation returns to zero, and the reverse flow persists in the boundary layer. Mei (1983) used the perturbation method to re-derive Keulegan's results. Liu & Orfila (2004) studied the boundary-layer flow under long waves in general, including the damping rates of solitary waves. Liu, Park & Cowen (2007) extended Liu & Orfila's (2004) linear solution and confirmed Keulegan's finding that the fluid velocity near the bottom reverses its direction and persists even long after the passage of the wave crest. Using particle image velocimetry (PIV), Lin *et al.* (2010) observed experimentally the velocity profile of the boundary layer induced by a solitary wave. Note that the foregoing results are for flows with 'thin' and laminar bottom boundary layers: i.e. the value of a/h_0 must be sufficiently large so that the viscous diffusion time scale is much greater than the wave time scale.

Liu (2006) studied the turbulent boundary-layer structure under arbitrary long waves by introducing the Boussinesq approximation and eddy-viscosity model. Vittori & Blondeaux (2008) modelled the boundary-layer flow field of a solitary wave by direct numerical simulation of the Navier–Stokes equations. Their results show that turbulent oscillations start to form after the passage of the wave crest, when the wave amplitude is larger than a critical value. They explained that the flow outside the bottom boundary layer decelerates after the passage of the wave crest, and an adverse pressure gradient appears in the boundary layer. The combination of the

decelerating flow and the adverse pressure gradient induces the flow instability in the bottom boundary layer that creates turbulence. Such results were demonstrated experimentally by Sumer *et al.* (2010), who observed the formation of a regular array of two-dimensional vortices; the vortices then become unstable, break, and produce small-scale turbulence.

For the case of a solitary wave, the water in front of the wave is quiescent; hence initially irrotational. Fluid rotation in the boundary layer commences as soon as the wave influences the bed. The vorticity-generation mechanism at a solid plane boundary can be obtained from the Navier–Stokes equations (Lighthill 1963). The conservation of linear momentum in the direction of wave propagation (or the flow in the x direction) on a no-slip flat stationary bed can be written exactly as

$$\frac{\partial \omega}{\partial z} = \frac{1}{\mu} \frac{\partial p_e}{\partial x}, \quad (1.2)$$

where ω is the vorticity in the y direction at the solid boundary $z = 0$ (note that the coordinate z points upward into the fluid domain from the horizontal bed, and a right-handed coordinate system is understood), μ is the dynamic viscosity, and $p_e = p + \rho g z$ is the excess pressure, with ρ the fluid density and p the pressure. If we approximate the pressure gradient in the x direction to be hydrostatic, $\partial p_e / \partial x \approx \rho g \partial \eta / \partial x$, the vorticity generation at the bed can be expressed as

$$\frac{\partial \omega}{\partial z} = \frac{\rho g}{\mu} \frac{\partial \eta}{\partial x}. \quad (1.3)$$

When a solitary wave propagates in the x direction, the water-surface elevation decreases in the x direction on the front face of the wave; hence $\partial \eta / \partial x$ is negative and the gradient of vorticity in the z direction at the bed must be also negative according to (1.3). Because the water ahead of the wave is quiescent (hence irrotational), positive vorticity (clockwise) must be generated at the bed and diffuses out to the fluid. The sign of vorticity is monotonic along the bed as the pressure increases in the front portion of the solitary wave. Behind the wave crest, $\partial \eta / \partial x$ becomes positive and the gradient of vorticity in the z direction must become positive on the bed; therefore, negative vorticity (counterclockwise) will be generated at the bed and diffuse into the fluid. Vorticity along the bed is also influenced by advection which is slower than the wave propagation. Because of this vorticity generation, diffusion and advection process, vorticity in the fluid along the bed could vanish somewhere along the lee side of the solitary wave. The point where the vorticity vanishes coincides with the point where the shear stress vanishes (see figure 1). For two-dimensional steady and incompressible flows, the location of vanishing shear stress is the point of either flow separation or attachment. This is often called Prandtl's separation criterion. The flow under a solitary wave is however not steady. For two-dimensional unsteady flows, the separation criterion is not as simple as Prandtl's criterion (see, for example, Sears & Telionis 1975; Williams 1977; Haller 2004). Nonetheless, inferring from Haller's (2004) kinematic analyses in the Lagrangian frame, the criterion ($\omega = 0$ at $z = 0$) should guide us to the approximate separation/attachment location. For a solitary wave, the sign change in vorticity along the boundary indicates flow attachment, because $\partial \omega / \partial x > 0$ at the point of $\omega = 0$ along the bed. There is no other critical point (i.e. separation) to form a separation bubble. This flow pattern is consistent with the persistent boundary-layer formation after the passage of the solitary wave

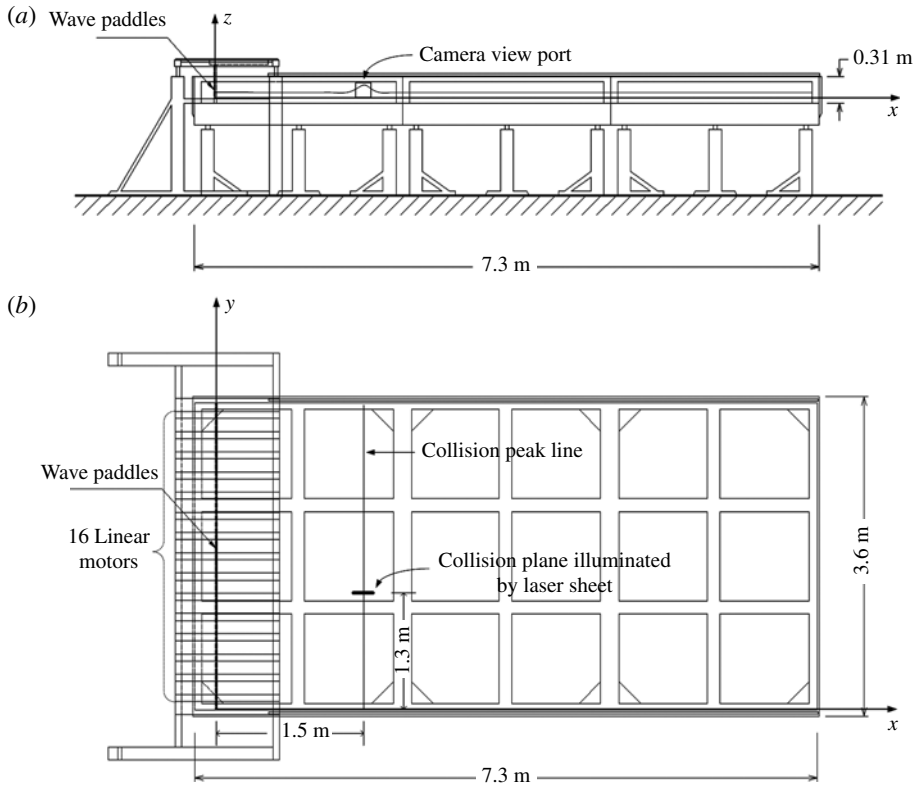


FIGURE 2. Schematic drawings of the wave basin. (a) Elevation view showing position of the camera view port. (b) Plan view showing the wave-maker generating two successive parallel waves. The coordinate system defined in the figure is used to describe the apparatus position.

as studied by Keulegan (1948). The boundary layer left behind the wave eventually diffuses out by viscosity, however.

The present research focuses on flows during the collisions of counter-propagating solitary waves, examining the evolution of the boundary-layer flow during the collisions. Contrary to the behaviour of a single solitary wave, it turns out that collisions of counter-propagating solitary waves induce flow separation.

2. Experiment set-up

Laboratory experiments are performed in a wave basin that is 7.3 m long, 3.6 m wide, 0.3 m deep, and elevated 1.2 m above the ground. Figure 2 depicts the experimental set-up. The origin of the coordinates is taken at the corner of the wave basin as shown in the figure; the x direction points horizontally along the sidewall, the y direction points perpendicularly away from the sidewall, and the z direction points upward. The wavemaker system is capable of generating arbitrarily shaped, multi-directional waves. With the use of 16 independently controlled linear-motor motion devices, each vertical wave paddle is pushed through hinge connections by two adjacent linear motors, and is moved horizontally in piston-like motions. To create counter-propagating solitary wave collisions, a pair of solitary waves are generated

in sequence with a certain time in between. When the first wave is reflected by the endwall and propagates backward toward the wavemaker, the second solitary wave is then generated so that these two waves collide at the specified location. The time interval between these two waves is controlled by the wavemaker control system. In the present experimental study, we set the collision location at $x = 1.5$ m and $y = 1.3$ m as shown in figure 2. Solitary waves are generated using the algorithm of Goring & Raichlen (1980), with the higher-order solution given by Grimshaw (1971). Detailed descriptions of the laboratory apparatus and procedures can be found in the companion paper Chen & Yeh (2014), hereinafter called Part 1.

To identify the experimental cases presented in this paper, the notation used in Part 1 is adopted. The head-on collision of two counter-propagating waves of equal amplitude is called a ‘symmetric head-on’ collision and that with unequal amplitudes is called an ‘asymmetric head-on’ collision. We also performed experiments for wave collisions with oblique angles. The results of the oblique collision cases are not reported herein, because the qualitative results do not differ from the head-on cases; the results and analyses for the oblique collisions can be found in Chen (2013).

Temporal and spatial variations of the water-surface profiles are captured with the laser-induced-fluorescent (LIF) imaging method as described in §3 of Part 1. To obtain the flow velocity data in the x – z plane (figure 2), PIV is used, which is a non-intrusive optical flow measurement system. A laser light sheet (Nd:YAG laser 190 mJ pulse⁻¹) illuminates a vertical plane in the flow, and the positions of seeded particles in that plane are recorded. A short time later, a subsequent laser pulse illuminates the same plane, obtaining a second set of particle images. From these sets of images, the velocity field is obtained by determining particle displacement over time. As is the standard practice, the raw PIV data are validated to remove outliers and smoothed to distribute the data at the grid nodes. Because the PIV images are taken sufficiently far away (1.3 m) from the sidewall, we used a telephoto lens (130 mm).

Similar PIV measurements for solitary waves were taken by Umeyama (2013). He reported however only one case of a head-on collision with small amplitude, $a/h_0 \approx 0.22$. His PIV measurements were made by emitting the laser sheet from above a narrow wave flume; hence the water-surface variation must necessarily have been small to minimize the laser-light refraction and scatter at the air–water interface. Perhaps this is the reason why his experiments were limited to a small-amplitude wave. No such restriction is applied to our laboratory experiments because the laser sheet is emitted through the transparent glass-plate bed from a position under the tank. To our knowledge, this study is the first of its kind in which the flow field is investigated to show the boundary-layer evolution during the collision of counter-propagating solitary waves.

Since the collision process is of short duration, the pulse frequency (14.5 Hz pulse rate) of the PIV system is not fast enough to obtain adequate temporal resolution for the transient process of wave collisions. To circumvent this problem, we repeat the experiment to fill the temporal gaps. With the aid of the high repeatability of our wavemaker system and the seamless synchronization of the wavemaker and PIV system, we repeat the experiment 28 times, shifting the triggering time of the PIV system by 5 ms. Since the original time lapse for one laser pulse is $1/14.5$ Hz ≈ 69.0 ms, the temporal resolution with two successive images is 138 ms. Repeating the experiment 28 times and integrating all the images, we produce image data every 5 ms. Frames 1 to 27 are at 5 ms intervals, then frame 28 has a 3 ms interval. The weighted-average smoothing procedure is used to correct these uneven time intervals. The Gaussian weighted average in time is applied to the time span of

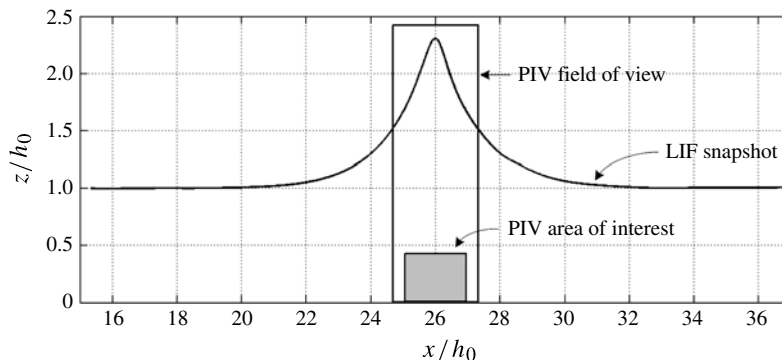


FIGURE 3. Measurement regions for LIF and PIV. The water surface is a snapshot of our LIF measurement for a symmetric head-on collision with the incident wave amplitude $a/h_0 = 0.52$. The large rectangle shows the field of view of our PIV camera. The grey shaded area shows the region of interest (ROI). We only process and present our PIV results within the ROI.

27 frames to produce the 200 Hz data with three frames set as the standard deviation of the Gaussian. Smoothing PIV data in space is a standard procedure; here we apply the same procedure in time. The experiments are precisely repeatable owing to our wavemaker system driven by the 16 linear motors: positional repeatability of the linear motor is $\pm 1.0 \mu\text{m}$ and temporal response resolution is 0.0625 ms. While the quantitative error analysis associated with this procedure is difficult, the performance of the linear motors should be adequate for the foregoing procedure to enhance the PIV temporal resolution. Furthermore, it will be shown in §4 that the resulting temporal variations of the flow field are smooth and coherent in time. Therefore, the performance of this technique to effectively increase the PIV temporal resolution turns out to be satisfactory.

Another difficulty of the PIV measurements is the limited resolution in space. The field of view of the PIV measurements is a square with 14.5 cm sides in order to maintain high resolution in the velocity-field data. The area is much smaller than for LIF measurements as illustrated in figure 3. While the collision point can be pre-determined and fixed in space for a symmetric collision, such a collision ‘point’ cannot be specified at a spatially fixed location for asymmetric collisions. For asymmetric collisions, the critical collision location with vanishing horizontal fluid-particle velocity does not stay in one place but moves during the collision process. It is therefore difficult to measure the transition of the velocity field in such a small area (~ 14.5 cm) of a single PIV field, while maintaining sufficient resolution. In order to capture the asymmetric collision process, we again repeat the experiment by taking three connected fields of measurement with an adequately overlapped measurement domain. It should be emphasized that this technique is possible in our experimental apparatus that has high repeatability even for creating asymmetric collision motions.

Because our focus is to study the flow field near the bottom boundary, we only process the data from the bed surface to $z = 2.52$ cm ($0 < z/h_0 < 0.42$), with a horizontal span of 10.2 cm ($\Delta x/h_0 = 1.70$) for symmetric collision cases. For asymmetric collision cases, the three sets of repeated experiments yield a vertical span of 2.82 cm ($0 < z/h_0 < 0.47$) and a horizontal span of 26.0 cm ($\Delta x/h_0 = 4.34$), attaining adequate overlap in the three sets of measurements. Note that, as shown

in figure 3, the data along the edges of the domain are not used for the analysis in order to avoid any uncertainty associated with the PIV data near the edges.

3. Data analysis

Once the two-dimensional velocity vector field in the x - z plane is obtained with the PIV system, we compute the corresponding acceleration and vorticity. The flow accelerations are obtained from our high-resolution velocity data in space and time (200 Hz). The local acceleration is calculated by central differencing in time. The advective acceleration is calculated from the central differencing scheme in space. The vorticity is computed from the velocity field by applying the central differencing scheme. In addition to the foregoing standard flow parameters, we apply a recently developed visualization technique by Zhang *et al.* (2009) for the velocity-gradient-tensor field to gain additional insights in the flow analysis.

It is well known that the fundamental information on flow kinematics, such as volumetric dilation, rotation, and angular deformation of an infinitesimal fluid lump can be extracted from the velocity-gradient tensor:

$$\frac{\partial u_i}{\partial x_j} = \frac{1}{N}(\nabla \cdot \mathbf{u})\delta_{ij} + \Omega_{ij} + \left(E_{ij} - \frac{1}{N}(\nabla \cdot \mathbf{u})\delta_{ij} \right), \tag{3.1}$$

where δ_{ij} is the Kronecker delta and N is the spatial dimension of the domain ($N=2$ or 3). In the first term on the right-hand side $\nabla \cdot \mathbf{u}$ represents volume dilation. The skew-symmetric tensor $\Omega_{ij} = (\nabla \mathbf{u} - (\nabla \mathbf{u})^T)/2$ represents fluid rotation (the superscript T denotes transpose) and vorticity can be extracted as a pseudo-vector. The last term includes $E_{ij} = (\nabla \mathbf{u} + (\nabla \mathbf{u})^T)/2$ which is symmetric and is the rate-of-strain tensor (or deformation tensor) that represents angular deformation of a fluid element. The velocity-gradient tensor is Galilean invariant, providing a significant advantage over analysis of the velocity-vector field itself, which is not Galilean invariant.

For a two-dimensional tensor field ($N=2; i=(1, 2); j=(1, 2)$), the velocity gradient can be represented by a 2×2 tensor and (3.1) can be expressed in the following normalized form:

$$T_{ij} = \frac{1}{A} \frac{\partial u_i}{\partial x_j} = \gamma_d \begin{pmatrix} 1 & 0 \\ 0 & 1 \end{pmatrix} + \gamma_r \begin{pmatrix} 0 & -1 \\ 1 & 0 \end{pmatrix} + \gamma_s \begin{pmatrix} \cos \theta & \sin \theta \\ \sin \theta & -\cos \theta \end{pmatrix}, \tag{3.2}$$

where T_{ij} is the velocity-gradient tensor normalized by its magnitude A (the square root of the dyadic product of the tensor itself), and $\gamma_d = (T_{11} + T_{22})/2$, $\gamma_r = (T_{21} - T_{12})/2$, $\gamma_s = (\sqrt{(T_{11} - T_{22})^2 + (T_{12} + T_{21})^2})/2$, $\theta = \arctan[(T_{12} + T_{21})/(T_{11} - T_{22})]$. The velocity-gradient tensor (3.2) can be expressed with the following parameters: the tensor magnitude A , the eigenvalues $\lambda_{1,2}$, and the eigenvectors. The eigenvalues $\lambda_{1,2}$ can be obtained from

$$\lambda_{1,2} = \begin{cases} \gamma_d \pm \sqrt{\gamma_s^2 - \gamma_r^2} & \text{when } \gamma_s^2 \geq \gamma_r^2, \\ \gamma_d \pm i\sqrt{\gamma_r^2 - \gamma_s^2} & \text{when } \gamma_s^2 < \gamma_r^2. \end{cases} \tag{3.3}$$

Because of the normalization by tensor magnitude A in (3.2), $\gamma_d^2 + \gamma_r^2 + \gamma_s^2 = 1$ and $\gamma_s \geq 0$. Note that eigenvalues become complex-valued when $\gamma_s^2 < \gamma_r^2$.

There are five idealized flow conditions to form the eigenvalue manifold: (i) pure positive scaling or pure volume dilation ($\gamma_d = 1, \gamma_r = \gamma_s = 0$), (ii) pure negative scaling or pure volume contraction ($\gamma_d = -1, \gamma_r = \gamma_s = 0$), (iii) pure counterclockwise

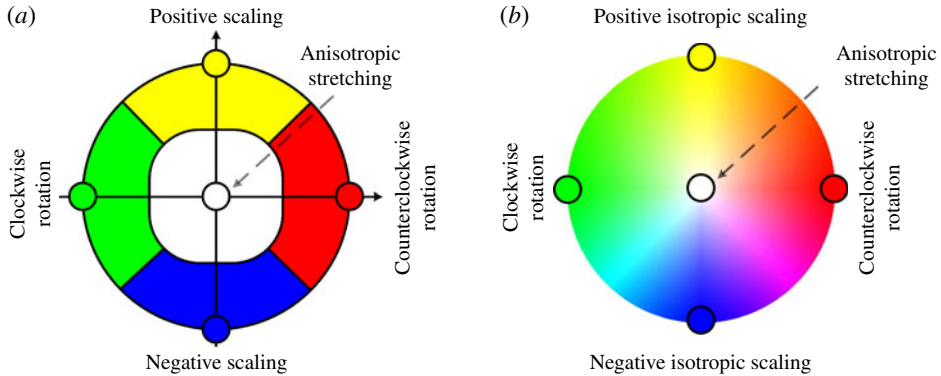


FIGURE 4. Eigenvalue manifold of the set of 2×2 velocity-gradient tensors. There are five distinct types of kinematics. (a) The five distinct kinematics with the Voronoi cells. (b) The unique colour assigned to every point in the eigenvalue manifold, mapped according to the colours and saturations.

rotation ($\gamma_r = 1, \gamma_d = \gamma_s = 0$), (iv) pure clockwise rotation ($\gamma_r = -1, \gamma_d = \gamma_s = 0$), and (v) pure angular deformation or anisotropic stretching ($\gamma_s = 1, \gamma_d = \gamma_r = 0$). In figure 4, those kinematic characteristics are visualized with mixtures of the following colours: (i) positive scaling (dilation) = yellow, (ii) negative scaling (contraction) = blue, (iii) counterclockwise rotation = red, (iv) clockwise rotation = green, and (v) angular deformation = white.

Unlike symmetric tensors, the major and minor eigenvectors of asymmetric tensors T_{ij} can be non-orthogonal when they are real-valued. Eigenvectors of the velocity-gradient tensor represent directions of stretching and compression. The eigenvectors of (3.2) only depend on γ_r, γ_s , and θ , and are independent of γ_d . Hence (3.2) can be re-normalized and expressed as

$$T(\theta, \varphi) = \sin \varphi \begin{pmatrix} 0 & -1 \\ 1 & 0 \end{pmatrix} + \cos \varphi \begin{pmatrix} \cos \theta & \sin \theta \\ \sin \theta & -\cos \theta \end{pmatrix}, \tag{3.4}$$

in which $\varphi = \arctan(\gamma_r/\gamma_s)$. The unit traceless tensor (3.4) can be represented as a unit sphere, which Zhang *et al.* (2009) consider as the eigenvector manifold as shown in figure 5. Zhang *et al.* further demonstrated that the topological behaviour of eigenvectors is dependent on the latitude φ only; hence (3.4) can be reduced for $\theta = 0$ to

$$T(\varphi) = \begin{pmatrix} \cos \varphi & -\sin \varphi \\ \sin \varphi & -\cos \varphi \end{pmatrix}, \tag{3.5}$$

which has two, one, or zero eigenvectors when $\cos 2\varphi > 0, = 0$, or < 0 , respectively.

Zheng & Pang (2005) classified the tensor state as (i) in the real domain, (ii) on the degenerate curve, and (iii) the complex domain. In the complex domain where both eigenvectors and eigenvalues are complex ($\gamma_s^2 < \gamma_r^2$ and $\pi/4 < |\varphi| < \pi/2$), Zheng & Pang introduced the concept of dual-eigenvectors, representing the elongation direction of the rotation dominant motion. From (3.5), it is clear that the equator $\varphi = 0$ represents the major and minor eigenvectors being orthogonal, meaning a condition of ‘pure shear’ with no rotation. When $\varphi = \pm\pi/4$, the major and minor eigenvectors coincide with each other, which represents a condition of ‘simple shear’.

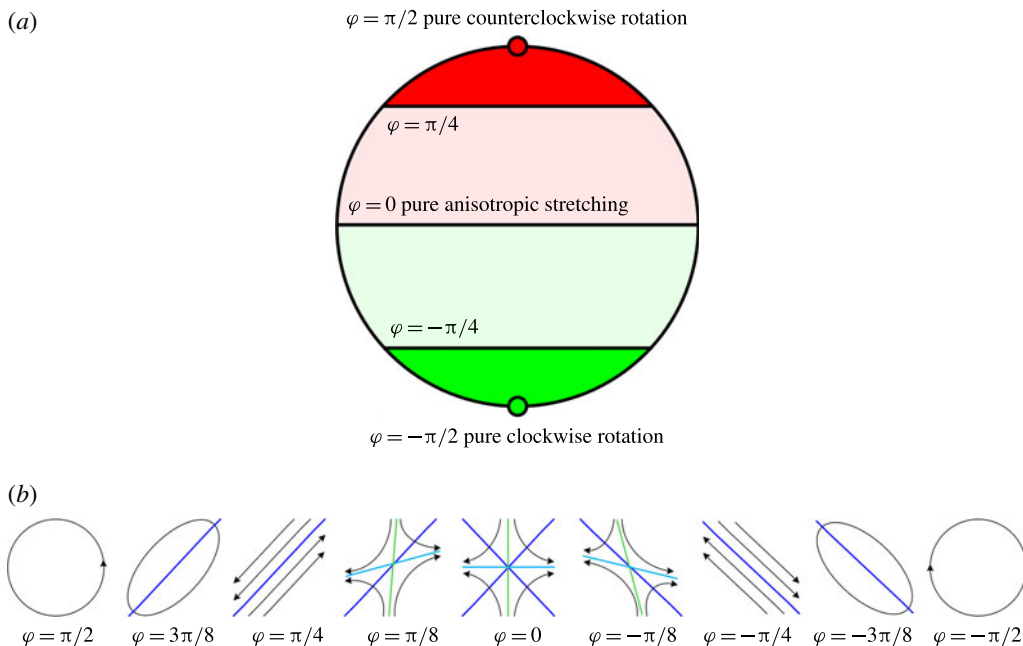


FIGURE 5. (a) Eigenvector manifold of the set of 2×2 velocity-gradient tensors. The orientation of the rotational component is counterclockwise in the northern hemisphere and clockwise in the southern hemisphere. Each hemisphere is partitioned into real domains and complex domains. The equator represents pure symmetric tensors (irrotational flows), the mid-latitudes ($\varphi = \pm\pi/4$) show simple shear flows; the poles represent pure rotations. (b) The relationship between the eigenvector manifold and the corresponding fluid deformation pattern.

At the location of $\varphi = \pm\pi/2$, the eigenvectors cannot be defined because of the state of pure rotation.

In our flow visualization, to express the directions of major and minor eigenvectors a pair of hyperstreamlines is used: note that hyperstreamlines are integral curves of eigenvectors in a second-order-tensor field (Delmarcelle & Hesselink 1993). On the other hand, the dual-eigenvectors are drawn in the complex domains ($\pi/4 < |\varphi| < \pi/2$) where fluid rotation dominates anisotropic stretching. The hyperstreamlines express the direction of stretching and compression, and the dual-eigenvectors represent the elongation of fluid rotation. The density of the hyperstreamlines represents the tensor magnitude A : the denser the hyperstreamlines, the larger the tensor magnitudes. This notion is analogous to the flow net (a graphical method used for the potential flow analysis): in the flow net, the distance between adjacent streamlines is proportional to the flow speed.

Figure 6(a) shows a snapshot of the velocity-gradient-tensor field near the bed (see figure 3) prior to the head-on collision of two identical solitary waves. The solid black lines represent the hyperstreamlines of the major eigenvectors, indicating stretching of the fluid elements in the vertical direction in the main flow domain and in the horizontal direction in the boundary layer, whereas the grey lines represent the hyperstreamlines of the minor eigenvectors, i.e. compressing the fluid elements in the horizontal direction in the main flow domain. This deformation pattern represents the pre-collision stage when the flow is converging from both horizontal directions and

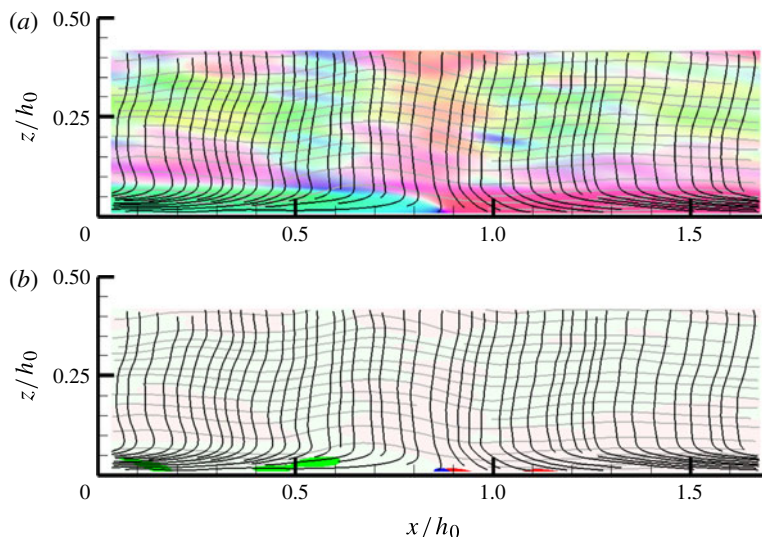


FIGURE 6. Combination of eigenvalue-based visualization and the hyperstreamlines representing eigenvectors and dual eigenvectors: yellow, dilation; blue, contraction; red, counterclockwise rotation; green, clockwise rotation; white, angular deformation. The black lines represent the major eigenvectors in the real domain and the dual eigenvectors in the complex domain, while the grey lines represent the minor eigenvectors. (a) Eigenvalue visualization based on the all-component (AC) method based on figure 4(b), showing smooth transition and relative strengths of (γ_d , γ_r , γ_s). (b) Visualization based on the dominant-component (DC) method, showing boundaries between regions with different dominant kinematic behaviour, as presented in figure 4(a): the real domain of the eigenvector manifold (figure 5) is also shown in faint green (clockwise rotation) and red (counterclockwise rotation).

the water-surface height is increasing. The spacing of the hyperstreamlines represents the tensor magnitude, presenting much higher magnitudes in the boundary layer. Also shown is the nearly irrotational flow away from the boundary, where the major and minor eigenvectors intersect each other nearly orthogonally and are shown in a light colour. A light colour expresses that anisotropic stretching (=‘white’) is dominant. Blue and yellow colours shown in figure 6(a) express flow contraction (negative scaling) and flow expansion (positive scaling), respectively, in the visualized two-dimensional plane. Because the water is incompressible, the expansion and contraction should be interpreted as the presence of flow gradients in the third dimension, i.e. the y direction. Note that the light-yellow regions and the light-blue regions are randomly mixed. Those areas represent unwanted small deviations (noise) from two-dimensional flow in the laboratory experiment. In the boundary layer, counterclockwise rotation (presented in red) with large magnitude (presented by dense hyperstreamlines) is shown under the left-running wave approaching from the right in the figure to the collision point, and clockwise rotation (presented by green) is shown under the right-running wave approaching from the left.

Figure 6(b) shows a snapshot of the same flow field as figure 6(a), but using a different visualization technique (see figure 4). While the visualization used in figure 6(a) allows for smooth transitions and preserves relative strengths of γ_r , γ_d , and γ_s , figure 6(b) explicitly depicts the boundaries between regions with different

dominant behaviours. Also indicated in figure 6(b) are the real domains of the eigenvector manifold, i.e. the domains where stretching dominates over rotation, and such domains are depicted in pale colours of green (clockwise rotation) and red (counterclockwise rotation). Following Zhang *et al.* (2009), we refer to the visualization of figure 6(a) as the AC (all-component) method, while the visualization used in figure 6(b) is called the DC (dominant-component) method. Figure 6(b) explicitly and correctly shows that the rotation-dominated regions occupy only small portions of the boundary layer. This does not mean that rotational motion in the boundary layer is small, but that anisotropic stretching (angular deformation) is equally important as rotation, representing the simple-shear-like flow in the boundary layer. The flow is nearly irrotational (white) in the domain above the boundary layer. Also, figure 6(b) shows no region in yellow or blue, except the very small spot in blue at the bed of the collision point that must be a stagnation point. This indicates that the flow expansion or contraction is indeed small and never dominates over other kinematics in the flow field which is designed to create a two-dimensional collision flow in the laboratory. The use of both AC and DC visualizations is complementary and leads to additional insights in the flow analysis.

4. Results

Water-surface variations in the collision processes are studied in Part 1. In that paper, the theoretical and numerical predictions of Su & Mirie (1980) and Craig *et al.* (2006) are verified quantitatively with precision experiments in the laboratory. Namely, wave amplification at the collision is larger than the sum of the two colliding solitary waves. After the collision, two counter-propagating waves regain their original solitary wave properties but with reduction of wave amplitudes. The collision also causes phase shift and generates trailing dispersive waves. These collision characteristics were realized in the laboratory water tank, and physical interpretations were given for important collision behaviours. In addition to head-on collisions, collisions with oblique angles were examined in § 4 of Part 1, and it was found that oblique collisions with small angles (less than 20°) have no significant differences from the equivalent head-on collisions.

4.1. Symmetric head-on collision

Figure 7 shows the measured water-surface variation during the head-on collision of two solitary waves. The measured amplitude of the right-running incident wave is $a/h_0 = 0.520$, while that of the left-running wave is $a/h_0 = 0.518$: the amplitudes are not exact but essentially the same, namely around $a/h_0 = 0.52$. The collision exhibited in figure 7 clearly demonstrates the phase shift and the generation of trailing dispersive waves. It is noted that this case is identical to the symmetric head-on collision of the highest waves discussed in figure 10 of Part 1. Here we focus on this large-amplitude case to study the flow field.

Figure 8 shows variations in the velocity field during the symmetric head-on collision: the corresponding water-surface variation is shown with solid lines in figure 9. Note that the time origin shown in figures 8 and 9 is at the maximum peak of the collision. The time intervals in figure 8 between the sets of plots (*a-i*) are not the same; the data were selected to present prominent features of the collision process. The top row of each figure set represents water-surface profile; the second row, the velocity field; the third row, the acceleration field; the fourth row, the vorticity field; and the fifth and sixth rows show the velocity-gradient-tensor field

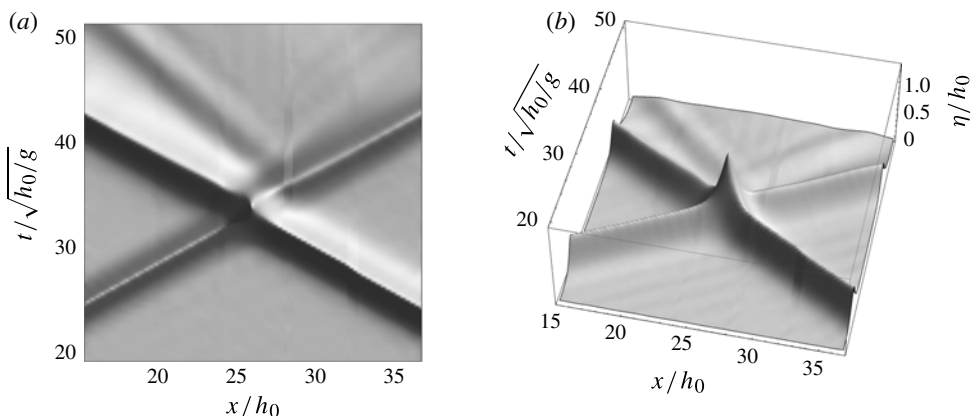


FIGURE 7. Two views of temporal variation of the water-surface profile in the x - z plane (parallel to the sidewall). The water depth is $h_0 = 6.0$ cm. The two colliding waves have equal wave amplitude $a/h_0 = 0.52$. The data were obtained by the LIF method.

with both visualization methods, namely the AC and DC methods, as discussed in §3. (Recall that the AC method depicts smooth transitions and relative strength of kinematics components, while the DC method allows for explicit boundaries between regions of distinct dominant kinematic behaviours.) All the plots cover flows in the range $0 < z/h_0 < 0.42$ and $0 < x/h_0 < 1.70$, except the vorticity plots which are distorted in the vertical range $0 < z/h_0 < 0.20$ in order to represent the vorticity in the boundary layer explicitly. The velocity field and acceleration field are displayed without spatial distortion by coupling the arrows and textures representing the vector field, and the colour code for the magnitude. Likewise, there is no spatial distortion to display the velocity-gradient-tensor fields because the relation between major and minor eigenvectors (i.e. the intersecting angles) is important for the analysis: recall that hyperstreamlines in the figures depict the directions of eigenvectors.

Figure 8(a) shows the pre-collision state: waves are approaching from both ends, and the velocities and accelerations are very small. The velocity-gradient-tensor field shows a somewhat random mixture of red (counterclockwise rotation), green (clockwise rotation), yellow (dilation), and blue (contraction). Anisotropic stretching (white) dominates over rotation in the majority of the flow domain as shown in the DC visualization: light green and light red regions (the real domain, see figures 4 and 5) dominate the dark green and red regions (the complex domain). The similar strengths of the red, green, yellow, and blue colours that appear in the AC visualization indicate that the magnitudes of these kinematic components are similar in the flow field. The incoherent and sparse pattern of hyperstreamlines indicates no organized flow and small tensor magnitude, although the major eigenvectors are somewhat oriented in the vertical direction, showing a precursor of the collision process.

Figure 8(b) exhibits flow activity: all the velocities point upward and toward the collision location. The pattern of flow acceleration also points upward and toward the collision point, except in the boundary layer. As shown in the arrow plot in figure 8(b), the acceleration in the boundary layer points downward (but still toward the collision point). This indicates that near the collision point, local pressure rise must be present away from the bed, which directs the neighbouring acceleration vectors downward. Vorticity in the boundary layer associated with incoming waves is counterclockwise (red) under the left-running incident wave and

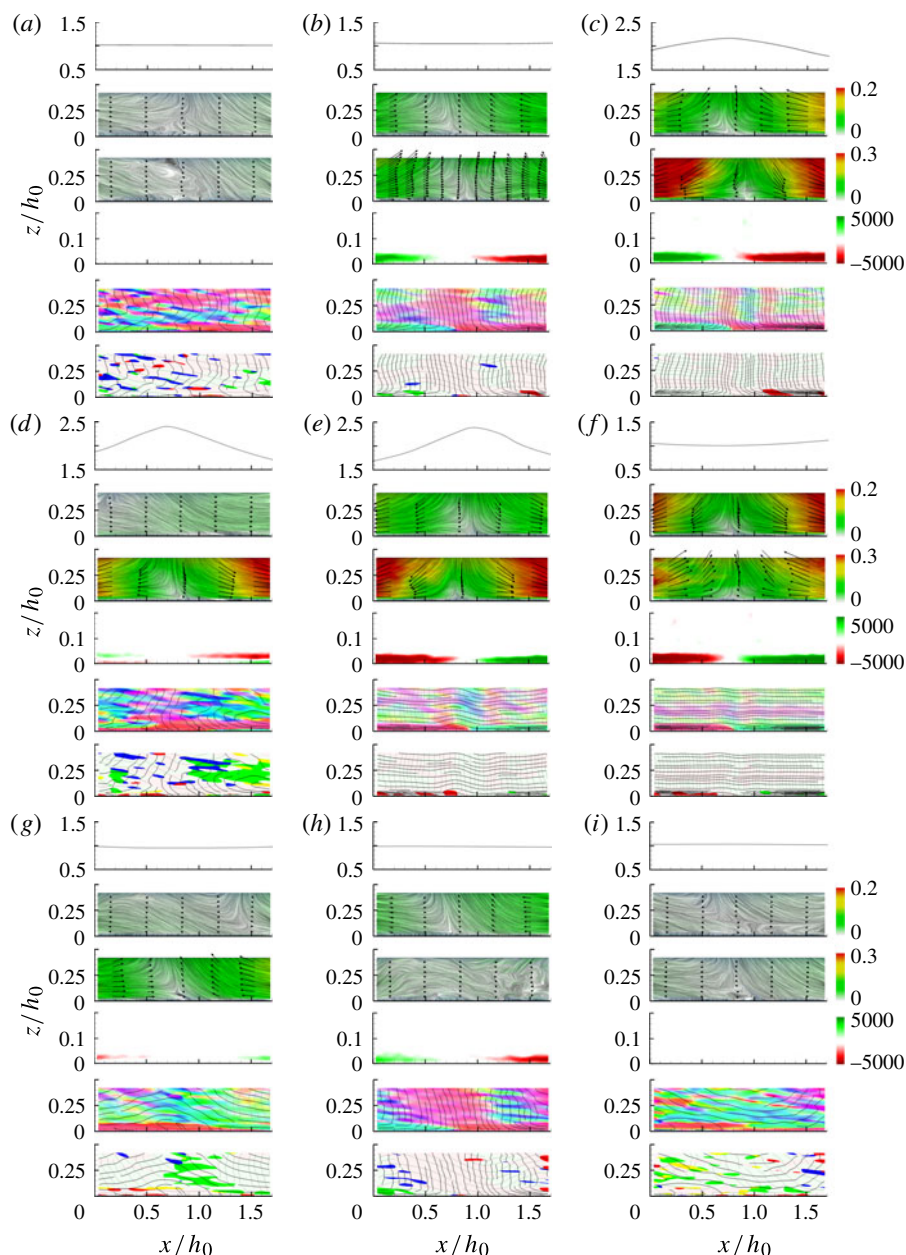


FIGURE 8. Time sequence of flow-field variations during the symmetric head-on collision of solitary waves in the domain $0 < z/h_0 < 0.42$ and $0 < x/h_0 < 1.70$: the origin of the local horizontal coordinate is equivalent to the global coordinate at $x/h_0 = 25.3$, see figure 3. The incident wave amplitude is $a/h_0 = 0.52$. In each of (a)–(i): first row, water-surface profile; second row, velocity field; third row, vorticity; fourth row, acceleration; fifth and sixth rows, AC and DC visualizations of the velocity-gradient-tensor field. (a) $t = -0.45$ s; (b) -0.30 s; (c) -0.05 s; (d) 0 s (at the peak of collision); (e) 0.05 s; (f) 0.25 s; (g) 0.35 s; (h) 0.45 s and (i) 0.65 s.

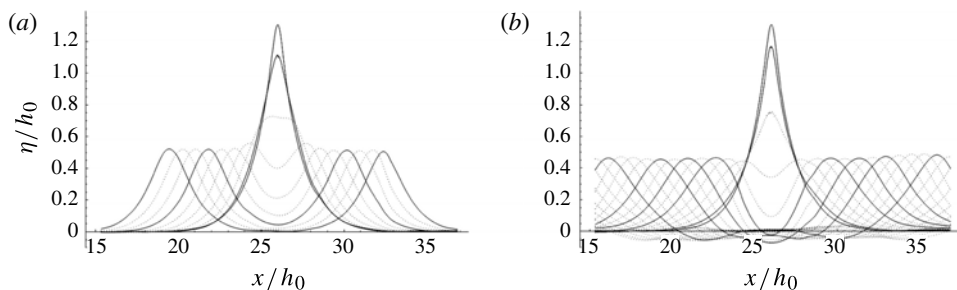


FIGURE 9. Waterfall plots of the temporal variation of the water-surface profile during the symmetric collision process for the incident wave amplitude $a/h_0 = 0.52$: (a) before the collision for 0.45 s, showing two approaching solitary waves; and (b) after the collision for 1.0 s, showing departing solitary waves. The time interval is 0.05 s. The data were obtained by the LIF method, and the solid lines represent the profiles that correspond to the velocity fields shown in figure 8: $t = -0.45, -0.30, -0.05,$ and 0 s in (a); and $t = 0, 0.05, 0.25, 0.35, 0.45,$ and 0.65 s in (b).

clockwise (green) under the right-running incident wave. The velocity-gradient-tensor field in figure 8(b) shows a coherent pattern of the hyperstreamlines; the major eigenvectors are oriented in the vertical direction and intersect nearly perpendicularly to the minor eigenvectors. This pattern indicates that the fluid is stretched in the vertical direction, and that the majority of the interior flow field is nearly irrotational; the exception is in the boundary layer where the tensor magnitude is greater than that in the interior domain (the closer the intervals between hyperstreamlines, the greater the tensor magnitude). The difference in colour contrast between the AC and DC visualizations still remains, although the contrast is less than the condition at $t = -0.45$ s (figure 8a), indicating that anisotropic stretching (white) becomes stronger than the other kinematic components.

Figure 8(c–e) shows the collision transition; the state of maximum wave amplification is shown in figure 8(d). (The peak wave elevation is shifted slightly in figure 8e due to a small mismatch in the incident wave amplitudes; as stated earlier, the measured amplitude of the right-running incident wave is $a/h_0 = 0.520$, while that of the left-running wave is $a/h_0 = 0.518$. Note that the shift of the peak location at $t = 0.05$ s from that at $t = 0$ s is very small and difficult to detect in the plots of figure 9b.) The velocity at the collision (figure 8d) is approximately nil everywhere, which means that the entire flow domain captured by PIV becomes nearly stagnant instantaneously. The acceleration points down and outward from the collision point. The vorticity in the boundary layer at the collision (figure 8d) exhibits a double-deck formation. On the right-hand side of the collision point, the counterclockwise rotation (red) that has been generated during the pre-collision process is diffused out to the interior, and clockwise rotation (green) is created underneath the counterclockwise rotation (red). The same occurs on the left-hand side of the collision, although the rotation directions are opposite. While the symmetrical head-on collision halts the fluid motion at $t = 0$ s, vorticity of opposite sign is created at the bed even before the initiation of the post-collision reverse flows. This can be readily explained by (1.3). At the collision, $\partial\eta/\partial x < 0$ on the right of the peak amplitude, while $\partial\eta/\partial x > 0$ on its left. According to (1.3), on the right-hand side of the peak, $\partial\omega/\partial z < 0$ at $z = 0$; hence, positive vorticity (clockwise direction) must be created at the boundary. The opposite holds on the right-hand side of the peak amplitude. After 0.05 s (figure 8e), the

vorticity pattern in the boundary layer becomes opposite to that in the pre-collision state (figure 8c).

It is emphasized that (1.2) is an exact consequence of the Navier–Stokes equation on a no-slip plane boundary, while (1.3) is an approximation of (1.2) assuming hydrostatic pressure along the bed. The deviation from this assumption can be evaluated by vertically integrating the Euler equation assuming the boundary layer to be thin:

$$p(x, z = -h_0, t) = \rho g(\eta + h_0) + \rho \frac{\partial}{\partial t} \int_{-h_0}^{\eta} w dz + \rho \frac{\partial}{\partial x} \int_{-h_0}^{\eta} u w dz, \quad (4.1)$$

where u and w are horizontal and vertical velocity components. Using the measured velocity field at the collision peak ($t = 0$ s), the ratio of the sum of the last two terms (vertical acceleration) of (4.1) to the first term (hydrostatic pressure) on the right-hand side is 0.053. Clearly, the effect of fluid acceleration on pressure is small enough to justify the use of (1.3).

Flow accelerations immediately before the collision (figure 8c) and immediately after the collision (figure 8e) are greater than that at the peak collision (figure 8d), especially in the region away from the collision point. Furthermore, it can be calculated with the measured data that vertically integrated acceleration over the depth along the crest at $t = 0.05$ s is 24% greater than that at $t = 0$ s. In spite of the limited area of the observation, the higher accelerations immediately before and after the peak collision are not consistent with the prediction for linear waves. Here we conjecture that this must be the effect of nonlinearity.

The collision process (figure 8c–e) in the velocity-gradient-tensor field reveals the kinematic transition behaviour. Figure 8(c) shows the same kinematic pattern as in figure 8(b) but much more persistent (0.25 s earlier than the timing of figure 8c); namely, stronger anisotropic stretching in the vertical direction in the interior domain and stronger tensor magnitude in the boundary layer. More important, the colour contrast in the DC and AC visualization methods becomes very similar in figure 8(c). This means that white further dominates the other colours (see figure 4); hence, anisotropic stretching dominates in the majority of the interior flow domain.

The velocity-gradient-tensor field suddenly becomes incoherent at the peak collision (figure 8d) with no dominant kinematic component in the field. This reflects the nearly stagnant state in the entire flow domain. Immediately after the collision (figure 8e), the flow in the interior region returns back to the state dominated by anisotropic stretching (the AC and the DC plots become similar to one another). As the two solitary waves start to move apart, the direction of the major eigenvectors becomes horizontal, instead of vertical as observed in the pre-collision state (figure 8b,c); fluid parcels are being stretched horizontally.

The post-collision process is shown in figure 8(f–i). There are two transitions in the flow pattern that we observed from the velocity-gradient-tensor plots. The first transition occurs at $t = 0.35$ s (figure 8g). The horizontally stretched pattern associated with the two solitary waves moving apart switches to stretching in the vertical direction at $t = 0.45$ s (figure 8h). This behaviour reflects the transition caused by the over-plunge of a falling wave after reaching maximum amplification at the collision (see figure 9b); the disturbance is local and is the cause of the generation of dispersive trailing waves. The over-plunging wave generates counterclockwise vorticity on the right and clockwise vorticity on the left, as shown in figure 8(h).

The velocity-gradient tensors allow us to identify one more transition process of the flow kinematics, which occurs at $t = 0.45$ – 0.65 s (figure 8h,i). Here, the

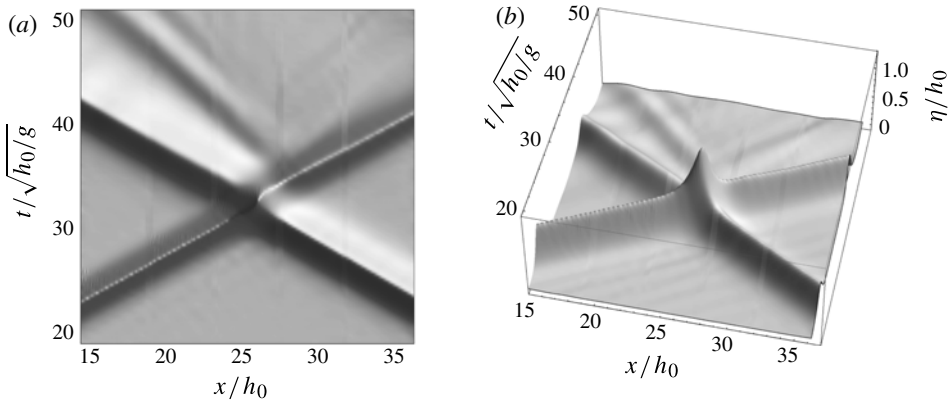


FIGURE 10. Two views of temporal variation of the water-surface profile in the x - z plane (parallel to the sidewall). The water depth is $h_0 = 6.0$ cm. The colliding two waves have unequal wave amplitudes $a/h_0 = 0.619$ and 0.413 . The data were obtained by the LIF method.

vertically stretched fluid parcels (shown by the vertically oriented major eigenvectors in figure 8*h*), resulting from the converging flows filling the dip caused by the over-plunge process, change to horizontally stretched (shown in figure 8*i*). This process generates the secondary dispersive trailing wave at the collision site: such a secondary wave generation can be detected in the water-surface profile shown in figures 7 and 9, although it is very small. The explicit identification of the flow patterns with hyperstreamlines is remarkable, demonstrating the usefulness of the velocity-gradient-tensor visualization. After this transition, the flow attenuates, and finally the tensor magnitude becomes very small, i.e. the density of hyperstreamlines becomes low. Visualization of the tensor field becomes incoherent, exhibiting a random mixture of the colours.

4.2. Asymmetric head-on collision

A collision of two solitary waves with different amplitudes (i.e. an asymmetric collision) is examined next. Temporal variation of the measured water-surface profile is recorded with the use of LIF technique, and the result is presented in figure 10. The amplitude of the right-running incident wave is $a/h_0 = 0.619$, while that of the left-running wave is $a/h_0 = 0.413$. Just like the head-on collision (figure 7), the collision process in figure 10 shows the phase shift and the generation of trailing dispersive waves.

Figure 11 shows the variations of the velocity field during the asymmetric head-on collision. The water-surface profile is shown in the top row; the velocity field in the second row; the acceleration in the third row; the vorticity in the fourth row; and the last two rows show the velocity-gradient-tensor field. (The format of the presentation is the same as that of figure 8.) Note that the corresponding water-surface profile of the collision process is shown in figure 12; the time origin is set at the instance of the maximum peak. Unlike symmetric collisions, an asymmetric collision cannot be identified as the occurrence at a single instantaneous time and at a certain fixed location; instead, the collision process is translated with the larger wave. Hence, it is necessary to take the data in a broader span in space to catch the collision process.

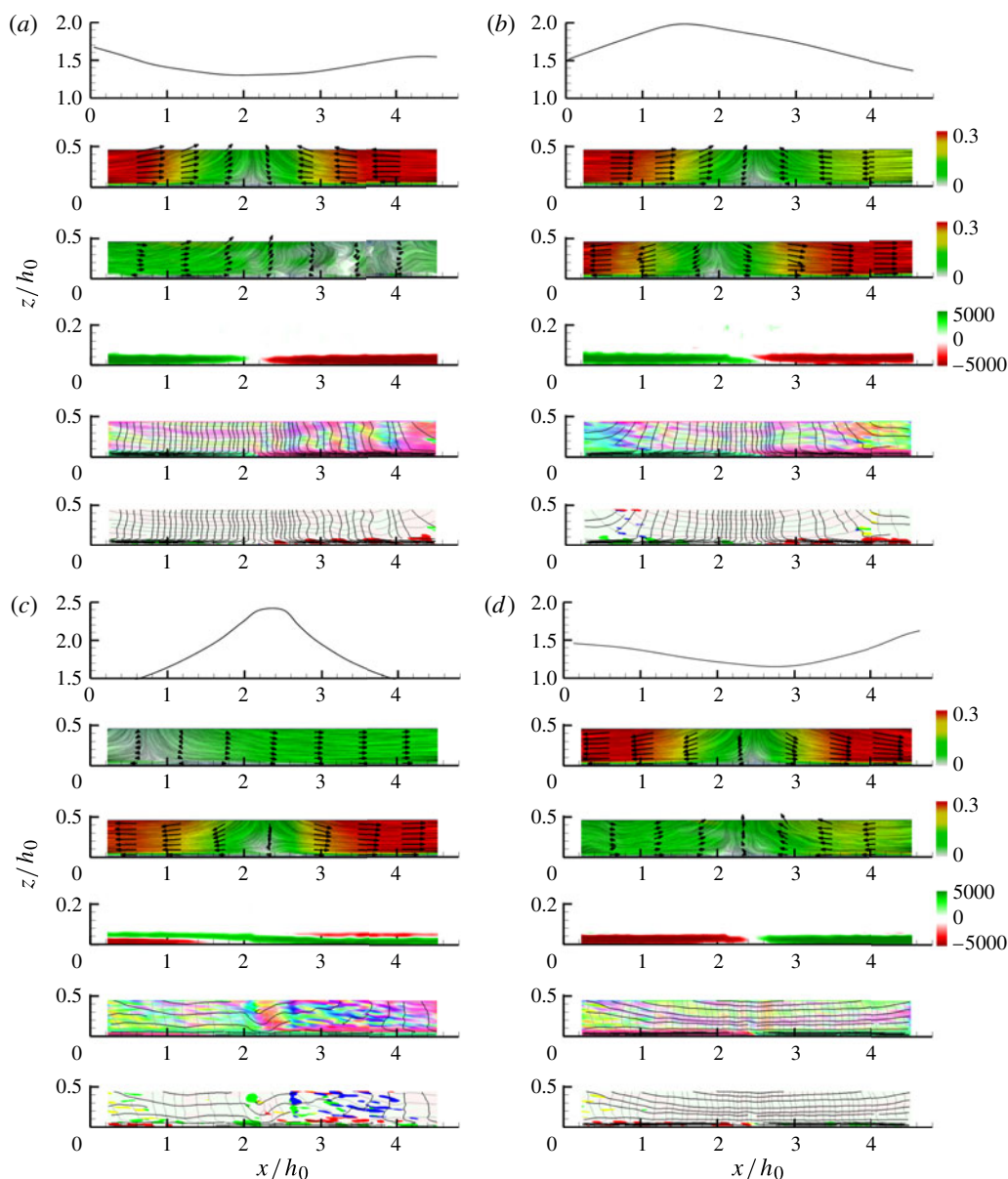


FIGURE 11. Time sequence of flow-field variations during the asymmetric head-on collision of solitary waves. The right-running incident wave has amplitude $a/h_0 = 0.62$ and the left-running wave $a/h_0 = 0.41$. Each set of plots was constructed as a montage of the data at three adjacent locations; the montage covers the area $0 < z/h_0 < 0.47$ and $0.209 < x/h_0 < 4.55$; the origin of the local horizontal coordinate is equivalent to the global coordinate at $x/h_0 = 23.8$, see figure 3. In each of (a–d): first row, water-surface profile; second row, velocity field; third row, acceleration; fourth row, vorticity; fifth and sixth rows, AC and DC visualizations of the velocity-gradient-tensor field. (a) $t = -0.2$ s; (b) -0.1 s; (c) 0 s (at the peak of collision); (d) 0.2 s.

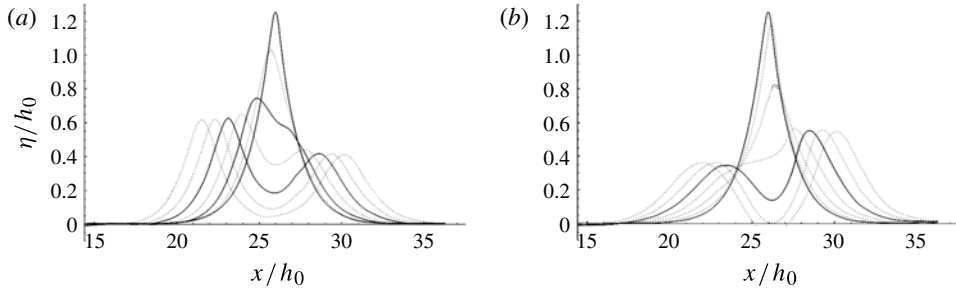


FIGURE 12. Waterfall plots of the temporal variation of the water-surface profile for wave amplitudes $a/h_0 = 0.619$ and 0.413 : (a) before the collision for 0.3 s, showing the two approaching solitary waves; (b) after the collision for 0.3 s, showing the departing solitary waves. The time interval is 0.05 s. The data were obtained by the LIF method, and the solid lines represent the profiles that correspond to the velocity fields shown in figure 11: $t = -0.2$, -0.10 , and 0 s in (a); and $t = 0$ and 0.2 s in (b).

To achieve this, we repeat the experiment by shifting the field of PIV measurement; three sets of slightly overlapped PIV data are taken and combined to make a montage just like the technique we used to obtain the water-surface profiles in a wider span. (It must be emphasized that the asymmetric collision process itself is highly repeatable in our precision experimental apparatus.) As discussed in § 3, the PIV measurement was repeated 28 times to gain sufficient temporal resolution. Consequently, we repeat the experiment $3 \times 28 = 84$ times to obtain the single set of data shown in each panel in figure 11.

Figure 11(a) shows the initiation of the collision. The velocity, acceleration, and vorticity plots represent the characteristics of approaching right-running and left-running solitary waves. Flow acceleration at this stage is small and asymmetric. Just like the symmetric collision (see figure 8*b,c*), the pattern of hyperstreamlines in the velocity-gradient-tensor field exhibits anisotropic stretching in the vertical direction that is associated with the converging flow prior to the collision. Figure 11(b) shows regions of weak tensor magnitude in the lee sides of both incoming waves, where the major eigenvectors (shown as dark hyperstreamlines) tend to become horizontal. Also of note is the variation of colour contrast between the AC and DC visualizations. In the middle of the domain, the colour contrast is similar between the AC and DC visualizations, while that is not the case in the end regions away from the collision. As we discussed regarding figure 8, the similar contrast means that the flow kinematics are dominated by the anisotropic stretching (angular deformation) in the middle of the collision process. These features are not captured in the head-on collision case presented in figure 8, because the horizontal span of the data is limited to $x/h_0 = 1.70$; we only took PIV measurements for a single measurement panel. On the other hand, figure 11 is a montage of three locations of frames of measurement.

The velocity stagnation point near the bed at $t = -0.20$ s (shown in figure 11*a*) is found at $x/h \approx 2.10$, whereas the stagnation point at $t = -0.10$ s (shown in figure 11*b*) is at $x/h_0 \approx 2.45$. This indicates that the collision point is moving with the larger solitary wave. Furthermore, significant magnitude of acceleration is detected in the regions away from the collision point in figure 11(b): it accelerates to the right in the right-hand region, and accelerates to the left in the left-hand region, indicating the effect of collision, i.e. decelerating flows by collision.

Figure 11(c) shows the moment of maximum amplification at $t = 0$ s. The velocity becomes small in the entire domain of measurement ($0.209 < x/h < 4.55$). The flow velocities point in the positive x direction except for the negligibly small velocity in the opposite direction in the far-left end of the domain. Flow acceleration becomes significant, maintaining the same pattern as that at $t = -0.10$ s (figure 11b). The vorticity pattern in the boundary layer exhibits the process of vorticity generation at the boundary and its diffusion, as described earlier. Vorticity at the bottom boundary – counterclockwise (shown in red) for the left-running wave and clockwise (green) for the right-running wave – diffuses out to the flow interior. When the collision occurs (figure 11b,c), the slope of water surface changes to $\partial\eta/\partial x < 0$ on the right of the collision spot and $\partial\eta/\partial x > 0$ on the left. Based on (1.3), these pressure gradients along the bed are responsible for the creation of the vorticity with opposite signs. Accordingly, the vorticity plot in figure 11(b) confirms $\partial\omega/\partial z < 0$ (increasing red colour from the bed) on the right-hand side ($\partial\eta/\partial x < 0$), and $\partial\omega/\partial z > 0$ (increasing green colour from the bed) on the left-hand side ($\partial\eta/\partial x > 0$). Figure 11(c) shows the more evident consequence with the appearance of the double-deck formation.

The velocity-gradient-tensor field shown in figure 11(c) presents some insightful features. First, notice that the tensor magnitude is small everywhere. The direction of major eigenvectors (stretching) is not uniform: the horizontal direction on the left-hand side and the vertical direction on the right-hand side. Although the magnitudes are small, flow convergence (blue) is present in the right-hand side of the domain, and flow divergence (yellow) appears in the left-hand side, which is opposite to the observation made in figure 11(b). Here we must emphasize that the experiment was designed for a square head-on collision. Therefore, the flow is supposed to be two-dimensional in the x - z plane with no dependence in the y direction. In spite of this set-up, the velocity-gradient tensor in figure 11(b,c) exhibits the features of isotropic scalings, which must be induced by flow convergence/divergence in the y direction. The reason is not clear, but it is attributed to a slight deviation from the perfectly two-dimensional wave motions in the real laboratory environment. Note that the laboratory experiments were performed in a wide wave basin (3.6 m wide with a water depth of 6.0 cm) and the measurements were made sufficiently far (1.3 m) from the sidewall. Hence, it is unlikely that the measurements were affected by the sidewall. There is no artificial flow confinement with sidewalls, which may allow minute lateral variations. Analysing all of our data (see Chen 2013), this experimental imperfection tends to appear only when the tensor magnitude is very small and in the following combination: positive scaling (expansion shown in yellow) arises when the flow is stretched in the horizontal direction, while negative scaling (contraction shown in blue) emerges when the flow is stretched in the vertical direction (compressing in the horizontal direction).

In the middle region of the tensor visualization in figure 11(c), we see the formation of an obliquely rising red blob (counterclockwise rotation) near $x/h_0 \sim 2.4$. This suggests flow separation. Also noticeable is the change in the behaviour of hyperstreamlines near the same location. The vorticity plot shows the layered formation of opposite vorticity in the boundary layer. Flow separation in steady two-dimensional flows on a plane boundary occurs where the vorticity vanishes, $\omega = 0$ and $\partial\omega/\partial x < 0$. The present flow is highly unsteady, however. Strictly speaking, Prandtl's separation criterion ($\omega = 0$ and $\partial\omega/\partial x < 0$ at the bed) is no longer applicable here. Nonetheless, the analysis by Haller (2004) suggests that Prandtl's criterion can still yield the approximate occurrence and the location of flow separation. When two solitary waves approach each other, vorticity on the bed changes from clockwise rotation (green) on the left of the domain to counterclockwise rotation (red) on the

right. Hence $\partial\omega/\partial x < 0$. This state indicates flow separation in the neighbourhood of $\omega = 0$. The vorticity plot in figure 11(c) shows that vorticity at the bed near the separation point is clockwise. Therefore, the flow separation must have taken place prior to the state of maximum amplification at $t = 0$ s (figure 11c). Once the vorticity pattern reverses as shown in figure 11(c), instead of separation, flow attachment should take place at the location of $\omega = 0$ and $\partial\omega/\partial x > 0$ (i.e. positive vorticity (green) on the right and negative vorticity (red) on the left of the figures). It is emphasized that the foregoing flow separation/attachment evaluations must be considered as approximations, because the collisions are unsteady.

Figure 11(d) shows the flow field of the rundown process after the collision. Just like the symmetric case shown in figure 8, the major eigenvectors become oriented in the horizontal direction, which reflects the flow field of the departing waves.

5. Conclusions

The flow-field transition processes during the collisions of counter-propagating solitary waves of large amplitudes are studied for two cases: (i) symmetric collision and (ii) asymmetric collision. The velocity fields are captured with the use of the PIV technique. Taking advantage of the precisely controlled laboratory apparatus with excellent repeatability, high-temporal-resolution PIV measurements (200 Hz) are achieved with standard PIV equipment by filling temporal gaps by repeating the experiment. The high-resolution velocity data enable us to accurately calculate flow acceleration, vorticity, and velocity-gradient tensors. Recently developed visualization techniques for asymmetric velocity-gradient tensors are applied to analyse the data.

Detailed transitional flow behaviour associated with the collisions is analysed with comprehensive examinations of velocity, acceleration, vorticity, and velocity-gradient-tensor data. For the symmetric collision case, the incoming solitary waves first ‘squash’ each other: consequently, the fluid parcels are stretched in the vertical direction. At the moment of collision, the flow halts instantaneously and uniformly. As the solitary waves move apart after collision, the fluid parcels are stretched in the horizontal direction. For the asymmetric collision case, we need to examine a broader domain because the collision takes place over some distance. Similar transitional flow behaviour as the symmetric case is observed but the process follows the motion of the larger solitary wave.

The following are some of the main findings from our observations. In the bottom half of the flow depth, maximum flow acceleration occurs immediately before and after the peak collision in areas slightly away from the collision point. This behaviour must be the effect of nonlinearity associated with the collision process. Characteristics and transition behaviour of vorticity in the bottom boundary layer are explained based on the vorticity-creation mechanism given by (1.2), assuming the pressure on the bed to be hydrostatic, estimated from the elevation of the water surface. This assumption was verified by computing the pressure at the bed by integrating the Euler equation vertically over the depth with the measured velocity data. The vorticity along the bed determines the occurrence of flow separation or attachment. While a single solitary wave propagating in quiescent water can cause flow attachment to the bed (not separation), a collision of counter-propagating solitary waves induces flow separation at the bed. A sign of flow separation is detected explicitly in the velocity-gradient-tensor field visualization during the asymmetric collision. Based on the generation–diffusion process of the vorticity on the bed, flow separation must occur at the stage prior to reaching the collision peak. After collision, flow attachment should occur at the bed instead. The formation of a dispersive wave train

after collision can be detected by the transitional behaviour of hyperstreamlines even when the absolute magnitude of measured velocities is small.

It is demonstrated that visualization of velocity-gradient tensors can express all the flow kinematics explicitly in the integrated presentation. The hyperstreamlines show that for both symmetric and asymmetric collision cases, the fluid parcels are stretched vertically prior to reaching the maximum amplitude. After the collision peak, fluid parcels are then stretched in the horizontal direction. The presentations of eigenvalues show explicitly that the flows induced during solitary-wave collisions are essentially irrotational, dominated by anisotropic stretching, except in the boundary layer. While the tensor magnitude is large in the boundary layer, anisotropic stretching and rotation are equally important there as shown by the patchy appearance of red and green in the background of white in the DC visualization (see figures 6, 8 and 11). In other words, the boundary layer is characterized as simple shear, as expected, that is represented at $\varphi = \pm\pi/4$ in figure 5. While most of the foregoing observations can be inferred from the basic fluid mechanics, visualization of the velocity-gradient-tensor field allows us to recognize the kinematics directly and explicitly.

Acknowledgements

This work was supported by Oregon Sea Grant Program (NA10OAR4170059-NA223L) and the Oregon State University Edwards Endowment. Y.C. is partially supported by the China Scholarship Council. The laboratory apparatus used in this study was designed by the late Professor J. Hammack.

REFERENCES

- CHEN, Y. 2013 Experimental study of counter-propagating solitary wave collisions. PhD thesis, Oregon State University.
- CHEN, Y. & YEH, H. 2014 Laboratory experiments on counter-propagating solitary wave collisions. Part 1. Wave interactions. *J. Fluid Mech.* **749**, 577–596.
- CRAIG, W., GUYENNE, P., HAMMACK, J., HENDERSON, D. & SULEM, C. 2006 Solitary water wave interactions. *Phys. Fluids* **18**, 057106.
- DELMARCELLE, T. & HESSELINK, L. 1993 Visualizing second-order tensor fields with hyperstreamlines. *IEEE Comput. Graph. Applics.* **13**, 25–33.
- GORING, D. & RAICHLIN, F. 1980 The generation of long waves in the laboratory. In *Proceedings 17th Intl Conference Coastal Engrs, Sydney, Australia*.
- GRIMSHAW, R. 1971 The solitary wave in water of variable depth. Part 2. *J. Fluid Mech.* **46**, 611–622.
- HALLER, G. 2004 Exact theory of unsteady separation for two-dimensional flows. *J. Fluid Mech.* **512**, 257–311.
- KEULEGAN, G. H. 1948 Gradual damping of solitary waves. *Natl Bur. Sci. J. Res.* **40**, 487–498.
- LIGHTHILL, M. J. 1963 Introduction: boundary layer theory. In *Laminar Boundary Layers* (ed. L. Rosenhead), pp. 46–113. Oxford University Press.
- LIN, C., HSIEH, S. C., YU, S. M. & RAIKAR, R. V. 2010 Characteristics of boundary layer flow induced by a solitary wave. In *Advances in Fluid Mechanics VIII* (ed. M. Rahman & C. A. Brebbia), pp. 267–279. WIT Press.
- LIU, P. L.-F. 2006 Turbulent boundary-layer effects on transient wave propagation in shallow water. *Proc. R. Soc. Lond. A* **462**, 3431–3491.
- LIU, P. L.-F. & ORFILA, A. 2004 Viscous effects on transient long-wave propagation. *J. Fluid Mech.* **520**, 83–92.
- LIU, P. L.-F., PARK, Y. S. & COWEN, E. A. 2007 Boundary layer flow and bed shear stress under a solitary wave. *J. Fluid Mech.* **574**, 449–464.

- MEI, C. C. 1983 *The Applied Dynamics of Ocean Surface Waves*. John Wiley & Sons, 740 pp.
- SEARS, W. R. & TELIONIS, D. P. 1975 Boundary-layer separation in unsteady flow. *SIAM J. Appl. Maths* **28**, 215–235.
- SU, C. & MIRIE, R. M. 1980 On head-on collisions between two solitary waves. *J. Fluid Mech.* **98**, 509–525.
- SUMER, B. M., JENSEN, P. M., SØRENSEN, L. B., FREDSE, J., LIU, P. L.-F. & CARSTENSEN, S. 2010 Coherent structures in wave boundary layers. Part 2. Solitary motion. *J. Fluid Mech.* **646**, 207–231.
- UMEYAMA, M. 2013 Investigation of single and multiple solitary waves using superresolution PIV. *ASCE J. Waterway Port Coastal Ocean Engng* **139**, 304–313.
- VITTORI, G. & BLONDEAUX, P. 2008 Turbulent boundary layer under a solitary wave. *J. Fluid Mech.* **615**, 433–443.
- WILLIAMS, J. C. 1977 Incompressible boundary layer separation. *Annu. Rev. Fluid Mech.* **9**, 113–144.
- ZHANG, E., YEH, H., LIN, Z. & LARAMEE, R. S. 2009 Asymmetric tensor analysis for flow visualization. *IEEE Trans. Vis. Comput. Graphics* **15**, 106–122.
- ZHENG, X. & PANG, A. 2005 2D asymmetric tensor fields. In *Proceedings 16th IEEE Conference Visualization, Vis'05*, pp. 3–10. IEEE Computer Society Press.